Journal Pre-proof

Tensile deformation behavior of a lightweight AlZnCu medium-entropy alloy

Sujung Son, Taek-Soo Kim, Soon-Jik Hong, Takayoshi Nakano, Hyoung Seop Kim

PII: S2238-7854(24)01515-1

DOI: https://doi.org/10.1016/j.jmrt.2024.06.204

Reference: JMRTEC 11147

To appear in: *Journal of Materials Research and Technology*

Received Date: 4 April 2024

Revised Date: 14 June 2024

Accepted Date: 27 June 2024

Tensile deformation behavior of a lightweight AlZnCu medium-entropy alloy

Sujung Son[a,b], Taek-Soo Kim[c], Soon-Jik Hong[d], Takayoshi Nakano[e], Hyoung Seop Kim[a,b,f,g,h,*]

[a] *Department of Materials Science and Engineering, Pohang University of Science and Technology (POSTECH), Pohang, 37673, Republic of Korea*

[b] *Center for Heterogenic Metal Additive Manufacturing, Pohang University of Science and Technology (POSTECH), Pohang 37673, Republic of Korea*

[c] *Korea Institute for Rare Metals, Korea Institute of Industrial Technology, Incheon 21999, Republic of Korea*

[d] *Division of Advanced Materials Engineering & Center for Advanced Materials and Parts of Powder (CAMP2), Kongju National University, Cheonan, 31080, Republic of Korea*

[e] *Division of Materials and Manufacturing Science, Graduate School of Engineering, Osaka University, 2-1 Yamadaoka, Suita, Osaka 565-0871, Japan*

[f] *Graduate Institute of Ferrous and Energy Materials Technology, Pohang University of Science and Technology (POSTECH), Pohang, 37673, Republic of Korea*

[g] *Advanced Institute for Materials Research (WPI-AIMR), Tohoku University, Sendai 980-8577, Japan*

[h] *Institute for Convergence Research and Education in Advanced Technology, Yonsei University, Seoul, 03722, Republic of Korea*

*Corresponding author: Hyoung Seop Kim

E-mail address: hskim@postech.ac.kr (H.S. Kim)

Abstract

Applying the medium-entropy alloy (MEA) concept to Al alloys is considered a promising approach to enhance their strength. However, achieving deformable Al-based MEA under tensile stress has not been reported due to the presence of a substantial amount of intermetallic compounds. Herein, we designed a novel AlZnCu MEA system and tailored its microstructure using high-pressure torsion, resulting in a meaningful tensile ductility of ~4.3% coupled with considerable tensile strength of ~462.5 MPa. The well-balanced tensile properties of the AlZnCu MEA stem from the nano-lamellar structure arising from phase separation and dispersion of discontinuous intermetallic compounds induced by the high-pressure torsion process.

Keywords: Aluminum alloys, Medium-entropy alloys, Nanocrystalline structure, Mechanical properties, Severe plastic deformation process

Impact statement

A deformable Al-based medium-entropy alloy under tensile stress was developed by a combination of thermodynamic calculation-based alloy design and thermomechanical processes.

Introduction

Aluminum alloys are attractive materials for diverse applications, such as automotive, aerospace, transportation, and portable devices, due to their inherent advantages of lightweight, specific strength, and corrosion resistance [1]. However, the low level of strength is the main stumbling block for aluminum alloys as structural materials. Various strengthening methods have been employed for aluminum alloys, such as solid solution strengthening, precipitation strengthening, dispersion strengthening, and grain refinement.

Recently, a new concept in materials science has emerged, involving high- and medium-entropy alloys (HEAs and MEAs), designed to improve mechanical properties [2]. HEAs and MEAs are designed to contain five or more metallic elements as principal elements, typically in equimolar or near-equimolar ratios. Due to the high configurational entropy, HEAs form single-phase solid solutions with substantial solid solution strengthening. Numerous metallurgists have adopted the HEA concept to conventional alloys, such as Fe and Ti alloys to improve diverse properties [3-6]. Al-based MEAs have also been attracting attention. For example, AlMgZnCuSi, AlCrCuMgSiZn, and AlCuMgSiZnZr systems were considered potential Al-based MEAs [7-10]. However, Zhang et al. added Zn and Cu to Al5083, achieving a higher yield strength [11]. Recently, Son et al. suggested a novel design strategy named the 'reverse approach', which involves the development of $Al_x(VCr)_{100-x}$ MEAs, starting from the Al-free V-Cr system [12].

Despite these advancements, the design of Al-based MEAs is still challenging due to the limited solubility of alloying elements in the Al matrix [12]. Among the alloying elements, Zn is one of the potential alloying elements due to its wide solubility in Al. Considering the binary system, the Al-Zn binary system can form a single solid solution with up to 67 at% of Zn [12,13]. Therefore, Zn can induce substantial solid solution strengthening in Al alloys. Copper, the main alloying element in the Al 2xxx series, can provide a substantial increase in strength and facilitate precipitation strengthening [14-16].

However, coarse and brittle precipitates can deteriorate the mechanical properties [5,9]. The fabrication of fine and distributed precipitates is one of the solutions for a good combination of strength and ductility. It is troublesome to roll the alloy with a large amount of precipitates for the refinement of the microstructure. However, high-pressure torsion (HPT), one of the severe plastic deformation (SPD) processes, can refine the microstructure without the risk of cracking, while also promoting materials flow and fragmentation of intermetallic compounds [17,18].

Herein, a novel AlZnCu MEA was designed and prepared by vacuum induction melting. Subsequent processing steps involving the HPT process and heat treatment were employed to precisely tailor the microstructure of the AlZnCu MEA. These procedures resulted in the creation of nanocrystalline microstructures and the disruption of coarse dendrites during the HPT process. As a result, balanced mechanical properties with high strength and ductility were achieved in the AlZnCu MEA under tensile stress.

Materials and methods

The $Al_{40}Zn_{40}Cu_{20}$ MEA was fabricated using a vacuum induction melting machine with mixtures of Al, Zn, and Cu elements, each possessing purity higher than 99.9%. The resulting as-cast ingot was machined into disks with diameters of 10 mm and thickness of 1.5 mm. Subsequently, the HPT process was conducted on the disks under a pressure of 6 GPa for 5 turns at a rotational rate of 1 rpm. Subsequent annealing was performed at 350 °C for 3, 10, and 60 mins within an Ar atmosphere, followed by water-quenching. The annealed samples were denoted as A3, A10, and A60, respectively.

The equilibrium phase diagram of the alloy was calculated using Thermo-Calc software with the SGTE database. Microstructural analyses were conducted by field emission-scanning electron microscopy (FE-SEM, JEOL JSM-7100F) and a scanning transmission electron microscope (STEM, JEM-2200FS). The elemental distribution of constituent phases was examined with backscattered electron (BSE) and energy dispersive spectroscopy (EDS) detectors equipped om FE-SEM and STEM.

Uniaxial tensile tests were conducted on dog-bone-shaped samples with gauge lengths of 1.5 mm, thicknesses of 0.7 mm, and widths of 1.0 mm. A quasi-static strain rate of 10^{-3} s^{-1} was applied, and the digital image correlation (DIC) method was used to measure the precise tensile strain. And, the compression tests were conducted on the cylinder-shaped specimen with a diameter of 4 mm and height of 6 mm. Deformed microstructures and fracture surfaces were subsequently observed and analyzed using FE-SEM.

Results and discussion

The design of the AlZnCu MEA began with the Al-Zn binary diagram [13]. The solubility of Zn in Al is 67 at%, which is a considerably high amount compared to those of other candidate elements such as Mg, Si, Mn, Cr, Fe, and V [12]. The increment of solid solution strengthening from the addition of alloying elements is one of the key advantages of HEAs and MEAs. The solid solution strengthening can be calculated by the following Fleischer's equation [19]:

$$\Delta\sigma_{ss} = \beta_i {x_i}^{1/2}, \tag{1}$$

$$\beta_i = 0.0045 G_{Al}(\eta_i' + 16\delta_i)^{3/2}, \tag{2}$$

$$\eta_i' = \frac{\eta_i}{1+0.5|\eta_i|}, \tag{3}$$

$$\eta_i = \frac{|G_i - G_{Al}|}{G_i}, \tag{4}$$

$$\delta_i = \frac{|a_i - a_{Al}|}{a_i}, \tag{5}$$

where $\Delta\sigma_{ss}$ is the amount of solid solution strengthening, and, β_i, x_i, η_i, δ_i, G_i, and a_i are the solid solution strengthening coefficient, atomic fraction, shear modulus misfit, atomic size misfit, shear modulus, and atomic size of element i, respectively (atomic size: 1.43 À for Al, 1.33 À for Zn, and 1.28 À for Cu, and shear modulus: 26.0 GPa for Al, 41.9 GPa for Zn, and 46.8 GPa for Cu [20]). As the amount of solid solution strengthening is proportional to the amount of solute contents according to equation (1), the higher solubility of alloying elements indicates higher solid solution strengthening. Therefore, Zn is an indispensable element in designing Al-based MEAs. The β_{Zn} is calculated to be 210.7 MPa from the higher shear modulus and smaller atomic size of Zn compared to Al. The amount of $\Delta\sigma_{ss}$ versus Zn concentration is displayed in Fig. 1. The $\Delta\sigma_{ss}$ is calculated as 148.3 MPa at 50 at% of Zn. As a result, Substantial solid solution strengthening was aimed for by mixing Al and Zn in equal proportions.

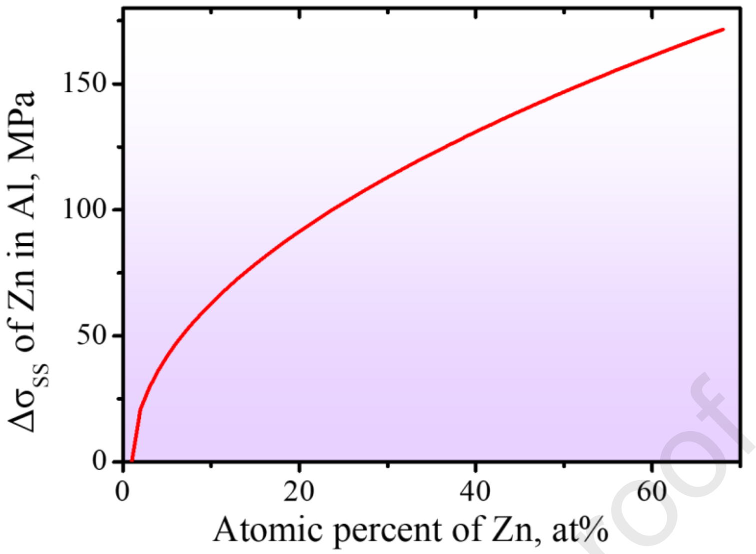

Figure 1. Solid solution strengthening induced by Zn addition to pure Al.

Copper, one of the most common elements in Al alloys, was introduced as a third constituent [14-16]. By adding Cu, the formation of Al-Cu precipitates is induced, leading to substantial precipitation strengthening in various Al alloys [21-23]. Furthermore, solid solution strengthening could be derived from a higher concentration of solute atoms, atomic size misfit, and modulus misfit [24]. Because Cu has a smaller atomic size than Al and Zn, with a higher shear modulus than Al and Zn, the β_{Cu} is calculated as 394.8 MPa [24], indicating significant solid solution strengthening can be achieved by Cu alloying in Al-Zn.

Figure 2(a, b) exhibits the equilibrium phase diagram of the AlZnCu alloy system with varying Cu contents. Without Cu, the AlZn alloy shows a wide FCC single-phase region. Meanwhile, the intermetallic compounds are formed with increasing the contents of Cu. To belong to the MEA regime based on a configuration entropy between 1.0R and 1.5R (R is the gas constant), AlZnCu alloys should contain Cu content over 14 at% [5]. And, to secure a two-phase region for feasibility in subsequent thermomechanical processes, Cu contents should be lower than 21.4% (Fig. 2(b)). Therefore, the nominal composition of $Al_{40}Zn_{40}Cu_{20}$ MEA was selected. Figure 2(c) displays the equilibrium phase diagram of $Al_{80-x}Zn_xCu_{20}$ alloy, which shows a miscibility gap. The miscibility gap leads to the phase separation of Al-rich and Zn-rich phases, similar to the miscibility gap in the binary Al-Zn alloy. In binary Al-Zn alloys, phase separation into Al-rich FCC and Zn-rich HCP phases is observed in Al-20Zn, Al-35Zn, and Al-49Zn alloys [13]. The phase separation can form profuse phase boundaries, enhancing mechanical properties [25,26]. To form profuse phase boundaries, the compositions of Al and Zn were set equal. As a result, the final composition of the $Al_{40}Zn_{40}Cu_{20}$ MEA has been established. The phase fractions of constituent phases in the $Al_{40}Zn_{40}Cu_{20}$ MEA at various temperatures from 0 to 1000 °C are displayed in Fig. 2(d). Because the two-phase region consisting of FCC and τ phase ranges from 323 to 383 °C, 350 °C was selected as the annealing temperature after the HPT process.

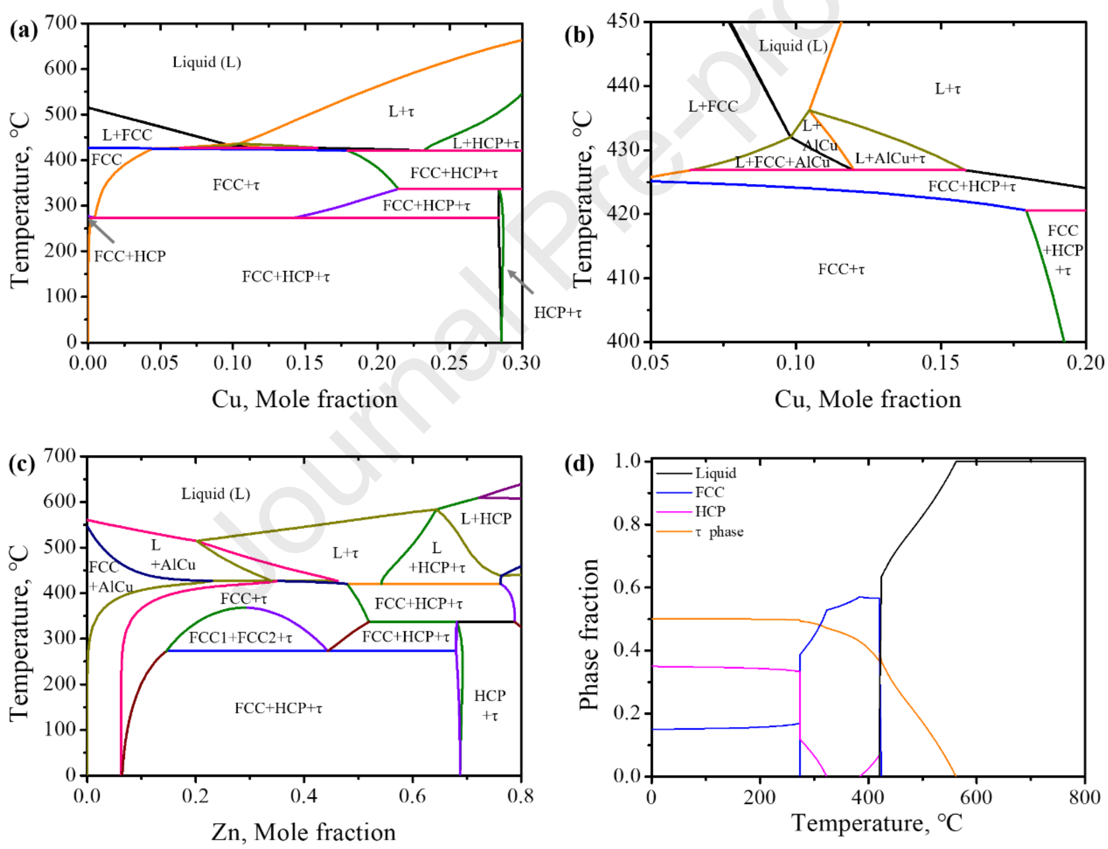

Figure 2. (a) Equilibrium phase diagram of the AlZnCu alloy system with varying Cu contents, (b) magnified phase diagram of the AlZnCu alloy, (c) phase diagram of the $Al_{80-x}Zn_xCu_{20}$ alloy with varying Zn contents, and (d) phase fraction as a function of temperature from 0 to 1000 °C.

After casting and the HPT process, the constituent phases in the AlZnCu MEA were analyzed by XRD patterns (Fig. 3). The as-cast sample contains four phases of FCC, HCP, AlCu, and Al_2Cu phases. Unlike the thermodynamic calculations, the AlCu and Al_2Cu intermetallic compounds formed rather than the τ phase. This discrepancy is attributed to the preference for Al-Cu bonding, given that the mixing enthalpy of the Al-Cu pair is the lowest value of -1 kJ/mol among the mixing enthalpy of others (Al-Zn: 1 kJ/mol and Zn-Cu: 1 kJ/mol) [27].

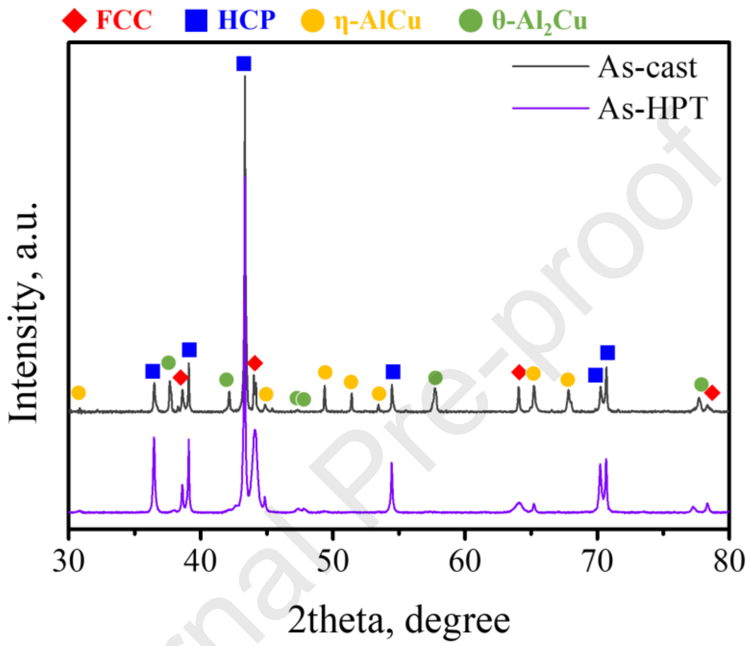

Figure 3. XRD patterns of the as-cast and as-HPT AlZnCu MEAs.

The distributions of phases and constituent elements in the AlZnCu MEA were analyzed by the low and high magnification BSE images with the corresponding EDS maps in Fig 4(a, b). In the as-cast microstructure, only three regions can be distinguished. The Al and Cu-rich grey dendrites are assumed to be AlCu intermetallic compounds, as expected in Fig.2(b). The black and white phases in the inter-dendrite regions are expected to be Al-rich FCC and Zn-rich HCP phases [13]. Because the melting temperatures of Al and Cu are higher than that of Zn, the Al and Cu-rich dendrites solidified first during solidification. The priority of solidification also suggests the formation of Al-Cu precipitates instead of the $Al_{34}Cu_{40}Zn_{20}$ phase [28]. And, the formation of Al, Cu-rich intermetallic compounds leaves the Al, Cu-lean liquid in the inter-dendrite regions. It means the composition of liquid shifts to the right side in Fig. 2(c), leading to the formation of the Zn-rich HCP phase. Therefore, the coarse HCP phase solidified, and fine lamellar structures of FCC and HCP phases were formed in the nanoscale, as shown in Fig. 4(b).

The coarse dendrite structure can lead to the continuous propagation of cracks and deteriorate the mechanical properties. To refine the microstructure, the HPT process was conducted on the as-cast disks. While there is no difference in constituent phases before and after the HPT process, the peak intensity of the Al_2Cu phase decreased after the HPT process. It is assumed that the Al_2Cu phases were dissolved during the HPT process [29]. Severe friction stress led to the fragmentation of precipitation and the increased interface energy of small precipitates provided a driving force of dissolution [30]. In addition, the peaks of the FCC phase were broadened due to grain refinement, lattice distortion, and stored strain induced by the SPD process [31]. From the BSE images of the as-HPT sample in Fig. 4(c), it was observed that the lamellar structures consisting of FCC and HCP phases were broken. Furthermore, the dendrites were mixed with the FCC and HCP phases, remaining some AlCu-islands smaller than 5 μm (Fig. 4(d)). Because there are different shear strains in the HPT-processed disk, the procedures of breakage and redistribution of AlCu dendrites can be investigated in Fig. S1.

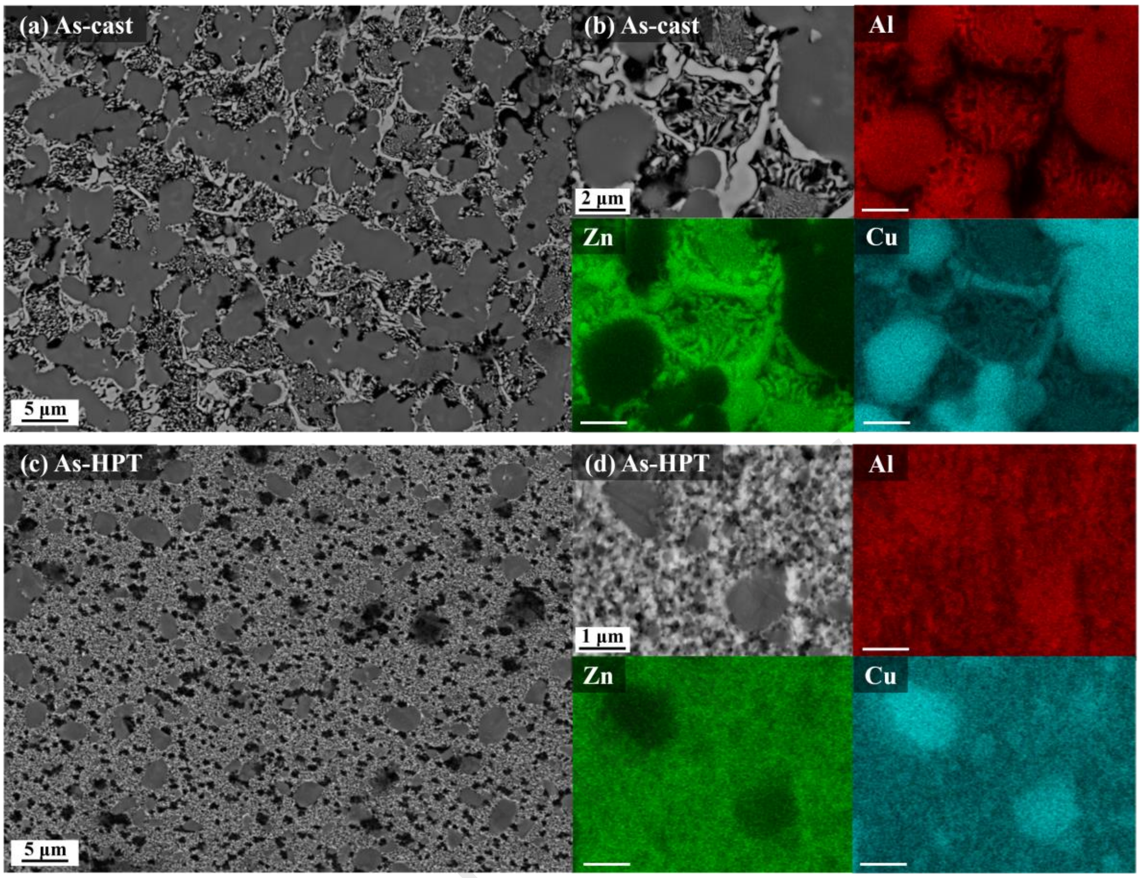

Figure 4. (a, c) Low and (b, d) high magnification SEM-BSE images of the (a, b) as-cast and (c, d) as-HPT AlZnCu MEAs with EDS maps of Al, Zn, and Cu.

As-HPT microstructures generally show ultrahigh strength with a sacrifice of ductility [31-33]. To mediate the strength and ductility, post-annealing was performed on the HPT-processed AlZnCu MEAs. Figure 5 shows the XRD spectra and BSE images of the annealed samples. After annealing, there was no difference in the constituent phases. However, recrystallization and recovery of deformed phases happen, as indicated by the sharpened peaks (Fig. 5(a)). The distributions of constituent phases are displayed in Fig. 5(b-d) and the phase fractions of each phase obtained from Fig. 5(b-d) is summarized in Table 1. As the annealing time increases, the phase fractions of AlCu and total HCP phases steadily increase. Meanwhile, the phase fraction of the FCC phase decreases from ~40.4 (A3), ~34.8 (A10), to ~32.4 (A60). This microstructural evolution can be elucidated by the dissolution during the HPT process [29,30]. The fragmentation and dissolution of intermetallic compounds during the HPT process result in the supersaturated FCC matrix [29,30]. And, the subsequent heat treatment can decompose the supersaturated FCC phases forming additional HCP and AlCu phases. Therefore, the phase fractions of AlCu and HCP phases steadily increase, while the phase fractions of FCC phase decrease. The other noticeable point is the selective grain growth during annealing (Fig. 5(b-d)). As the annealing time increases from 3 to 60 min, the growth of HCP and AlCu phases is distinctly observed. The grain sizes of island HCP phases increase from ~0.70 (A3), ~1.06 (A10), to ~1.60 μm (A60). The growth of AlCu phase proceeds more rapidly (~0.73, ~1.50, and ~5.92 μm for A3, A10, and A60, respectively). However, the FCC and HCP phases in the lamellar structure still remain as nanocrystalline structures with grain sizes lower than 200 nm. This is because the phase boundary in the lamellar structure acts as a strong obstacle to grain growth [13,34]. Furthermore, the HCP and AlCu phases in the A60 sample coarsened and became interconnected, while the HCP and AlCu phases in the A3 and A10 samples remained as islands surrounded by FCC and HCP lamellar structures.

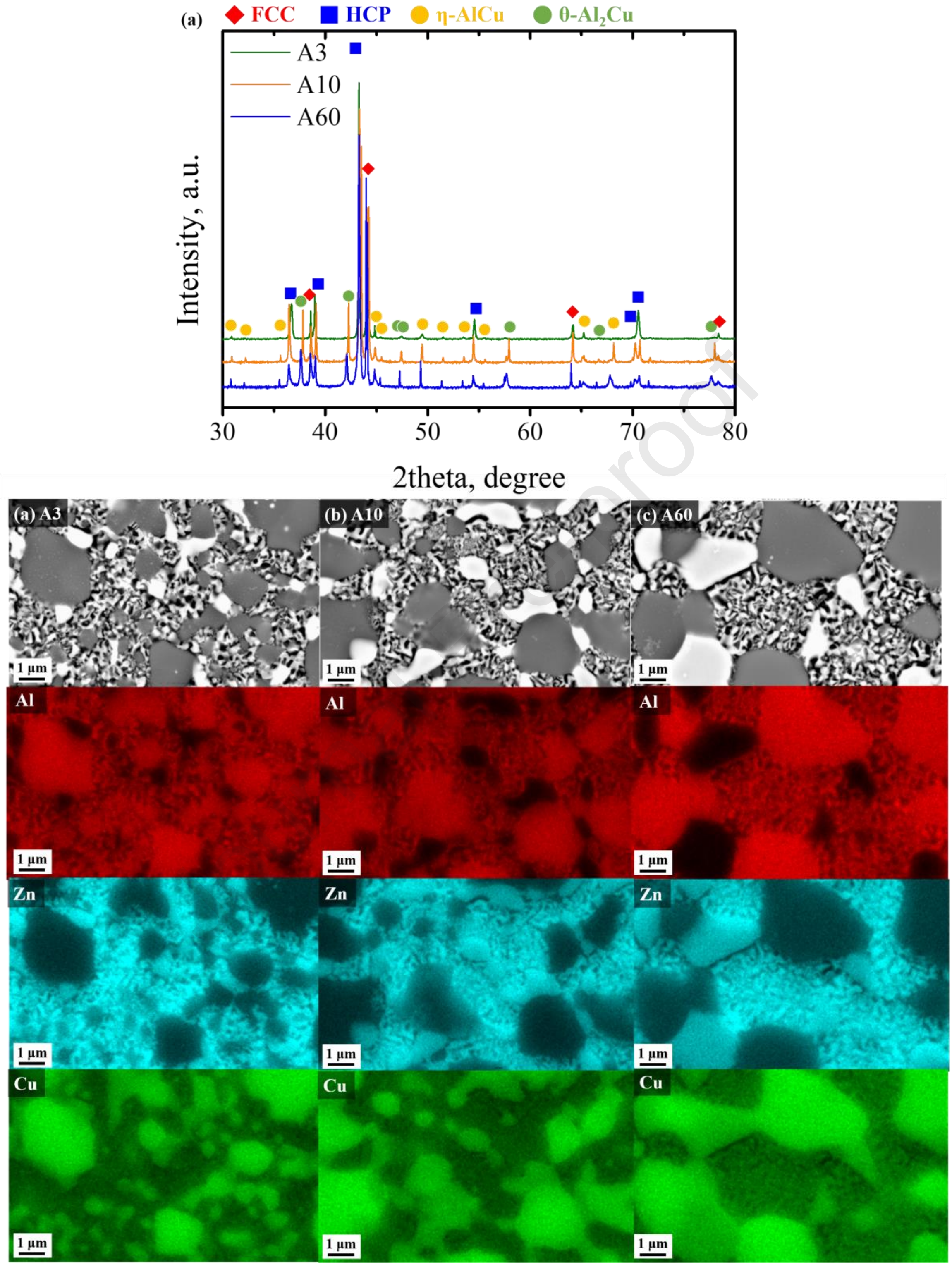

Figure 5. (a) XRD patterns of annealed AlZnCu MEAs and SEM-BSE images with EDS maps of Al, Zn, and Cu of (b) A3, (c) A10, and (d) A60.

Table 1. Volume fractions of the constituent phases in the annealed AlZnCu MEAs.

vol%	AlCu	FCC	HCP		
			Island HCP	Lamellar HCP	Total HCP
A3	~37.0	~40.4	~6.3	~16.3	~22.6
A10	~38.7	~34.8	~10.9	~15.6	~26.5
A60	~39.8	~32.4	~10.6	~17.2	~27.8

To clarify the regional composition and crystal structures of constituent phases, TEM analysis was conducted on the A10 sample (Fig. 6). The four phases were clarified based on the elemental distribution in Fig 6(a). The overall and regional compositions in Fig. 6 are summarized in Table 2. The overall Zn content slightly decreases compared to the nominal composition due to Zn evaporation, attributed to its low melting point. In Fig. 6(a), the black phase labeled 'A' mainly consists of the Al element with small amounts of Zn and Cu as solutes. From the SAED pattern from region A (Fig. 6(b, f)), the Al-rich phase is confirmed to be an FCC structure. Due to the small atomic sizes of Zn and Cu, the lattice parameter slightly shrinks to ~4.03 Å compared to 4.05 Å of pure Al [35]. Meanwhile, the white regions are divided into 'B' and 'C'. Region B is enriched in Zn, while region C is enriched in Al and Cu. Region B is composed of 83 at%Zn, 15 at%Cu, and 2 at%Al. Based on the binary phase diagram of the Zn-Cu system [36], the HCP structure is stable. The SAED in Fig. 6(g) exhibits of HCP phase with a zone axis of [110]. The lattice parameter (a: 2.57 Å and c: 4.78 Å) obtained from the SAED pattern also shrinks compared to those of pure Zn (a: 2.66 Å and c: 4.95 Å [37]), which is affected by small Cu solutes. Region C, with higher Cu contents than region B, is assumed to be the θ-Al_2Cu phase (Fig. 6(d). Figure 6(h) displays the SAED patterns of Al_2Cu related to the [110] zone axes [38,39]. Also, the ratio of Al to Cu is almost 2, which supports that intermetallic compounds are the θ-Al_2Cu phase. The grey region D possesses the highest amount of Cu, similar to the amount of Al. It is reported that AB-type transition metal aluminides generally have a B2 structure [40]. Also, the SAED pattern obtained from region D supports the BCC structures with [110] zone axis. While the AlCu phase exhibits B2 ordering [41-43], there is no superlattice peak of the B2 phase in Fig. 6(i). This is because the addition of Zn increases the mixing entropy, stabilizing the disordered structure. Also, the mixing enthalpies of Al-Zn and Zn-Cu are positive values, weakening the chemical ordering.

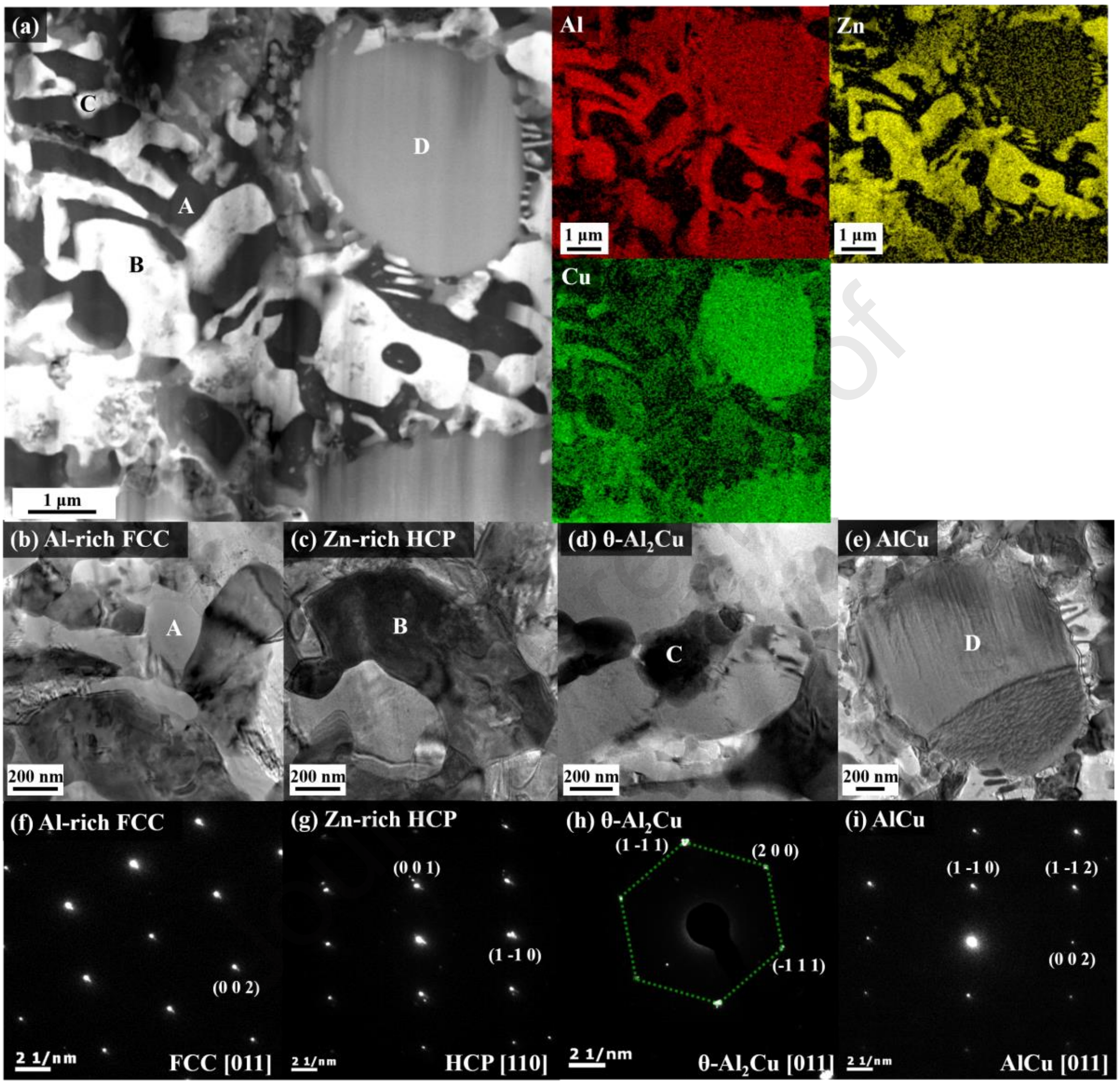

Figure 6. (a) TEM micrographs of the A10 sample with the corresponding EDS maps of Al, Zn, and Cu, (b-e) enlarged TEM images, and (f-i) SAED patterns obtained from (b-e), respectively. The SAED patterns were obtained from the labeled phase in TEM images (A: Al-rich FCC, B: Zn-rich HCP, C: θ-Al_2Cu, and D: AlCu).

Table 2. Overall and regional compositions of the AlZnCu MEA as determined from the image in Fig. 6(a).

	Atomic percent, at%		
	Al	Zn	Cu
overall	43.2 ± 0.2	36.0 ± 0.9	20.8 ± 0.7
FCC (A)	96.2 ± 0.1	0.5 ± 0.1	3.3 ± 0.3
HCP (B)	2.0 ± 0.1	83.0 ± 0.1	15.0 ± 0.3
θ-Al_2Cu (C)	61.6 ± 0.4	3.4 ± 2.2	35.0 ± 1.7
AlCu (D)	53.0 ± 0.7	5.7 ± 0.3	41.3 ± 0.9

The AlZnCu MEA possesses the Al-rich FCC, Zn-rich HCP, AlCu BCC, and Al_2Cu phases. The complicated microstructure provides profuse phase boundaries, which can contribute to strengths significantly. Furthermore, the phase separation of FCC and HCP phases induced by a miscibility gap forms nanocrystalline microstructures and effectively suppresses grain growth, which preserves mechanical properties during the annealing [44].

To evaluate the mechanical properties of AlZnCu MEAs, tensile tests were performed on the cast and annealed AlZnCu MEA (Fig. 7(a)). Under tensile stress, the as-cast sample shows a catastrophic fracture before yielding. However, the cast sample can withstand tensile stress up to 357.0 ± 5.1 MPa, which is noticeable considering that the yield strength (YS) of Al alloys varies from 100 to 650 MPa [1,45-47]. After the HPT process and subsequent annealing, the maximum stress increases due to the fine lamellar structures and well-distributed intermetallic compounds. Furthermore, the A3 and A10 samples show plastic deformation after yielding. The plastic deformation in the A3 sample is negligible with a total elongation of 1.3 ± 0.2%. However, the YS of the A3 sample rises to 360.5 ± 12.4 MPa. Meanwhile, the A10 sample definitely exhibits plastic deformation up to a total elongation of 4.3 ± 0.7% and achieves the highest YS of 408.7 ± 16.2 MPa and ultimate tensile strength of 462.5 ± 25.1 MPa. The Vickers hardness of AlCu intermetallic compounds is ~411 Hv, which is much higher than those of Al (~48 Hv) and Zn (~43 Hv) [48-50]. Although the grain size of constituent phases grows during annealing, the A10 exhibits the highest YS due to the higher amount of hard AlCu phase (Table 1). However, brittle fracture happens again in the stress-strain curve of the A60 sample.

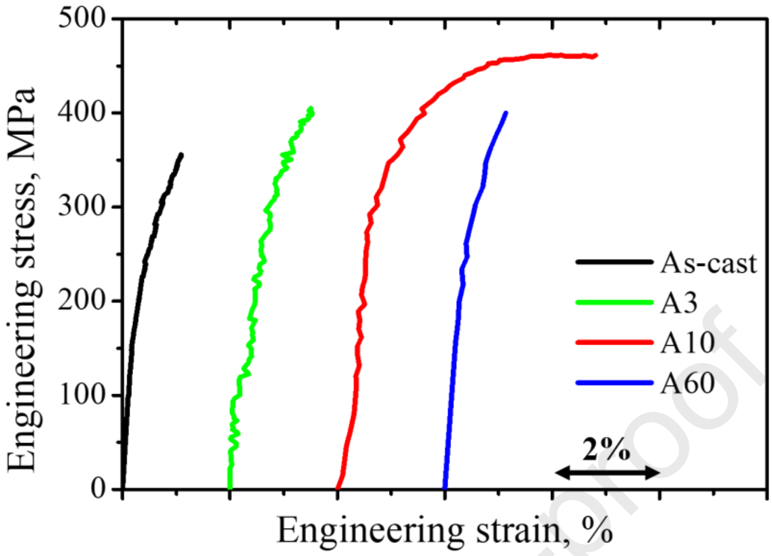

Figure 7. Engineering stress-strain curves of the as-cast, A3, A10, and A60 samples.

To describe the tensile behavior of AlZnCu MEAs, SEM analysis on the fracture surface of the deformed A10 sample was conducted. The overall fracture surface in Fig. 8(a) is composed of small facets due to the nanoscale grain size of the A10 sample. When the fracture surface is magnified in Fig. 8(b), the fracture morphologies of both ductile and brittle fractures are observed. First, the smooth surface indicated by the blue arrow exhibits river patterns, which is obvious evidence of brittle fracture [26]. The brittle fracture occurs in the Al Cu intermetallic compounds due to its lack of ductility. Meanwhile, the lamellar structures positioned between AlCu phase are indicated by the black arrows, which shows the ductile dimple fracture. According to the microstructural evolution and fracture morphologies, the hard AlCu phases contribute to the high YS and the ductile lamellar structures preserve the ductility of AlZnCu MEAs.

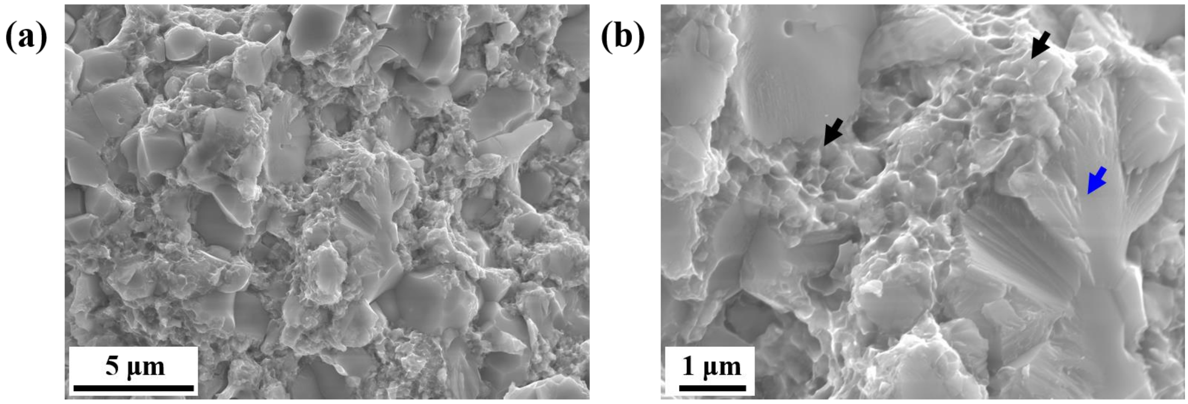

Figure 8. Fracture surfaces of the fractured A10 sample with (a) low magnification and (b) high magnification. The black and blue arrows indicate the fracture morphologies of dimples and river patterns, respectively.

Furthermore, longitudinal sections of the fractured samples were observed to show the propagation of cracks in the AlZnCu MEAs with different process conditions. Figure 9(a) shows the fractured as-cast sample. In the as-cast sample, the crack indicated by a red arrow initiates at the brittle AlCu phase and easily propagates along to coarse AlCu dendrite structure [51,52]. Meanwhile, the AlCu phase in the A3 samples becomes smaller during the HPT and annealing process. In Fig. 9(b), the cracks in the A3 samples proceed through the fragmentation of the AlCu phase and phase interfaces. Due to nanostructures in the A3 sample, the crack severely detours. However, the annealing time of 3 min is not enough to recover the deformation from the HPT process. The deformed HCP phase and lamellar structure cannot withstand substantial tensile deformation, which leads to a small elongation of ~1.3%. The A10 sample shows the largest elongation, which stems from the recovery of FCC and HCP phases and the fine AlCu phases. The recovered FCC and HCP phases of the A10 sample can withstand deformation, leading to crack tip blunting and delaying the crack propagation [53]. Also, the lamellar structure of AlZnCu MEAs effectively blocks crack propagation. In Fig. 9(c), the yellow arrows indicate cracks arrested by ductile lamellar structures, leading to an enhanced elongation of ~4.3% [54,55]. In contrast, the elongation of the A60 sample catastrophically decreases. This is because the overgrown AlCu phases in the A60 sample offer a continuous path for crack propagation, as indicated by the red arrow in Fig. 9(d).

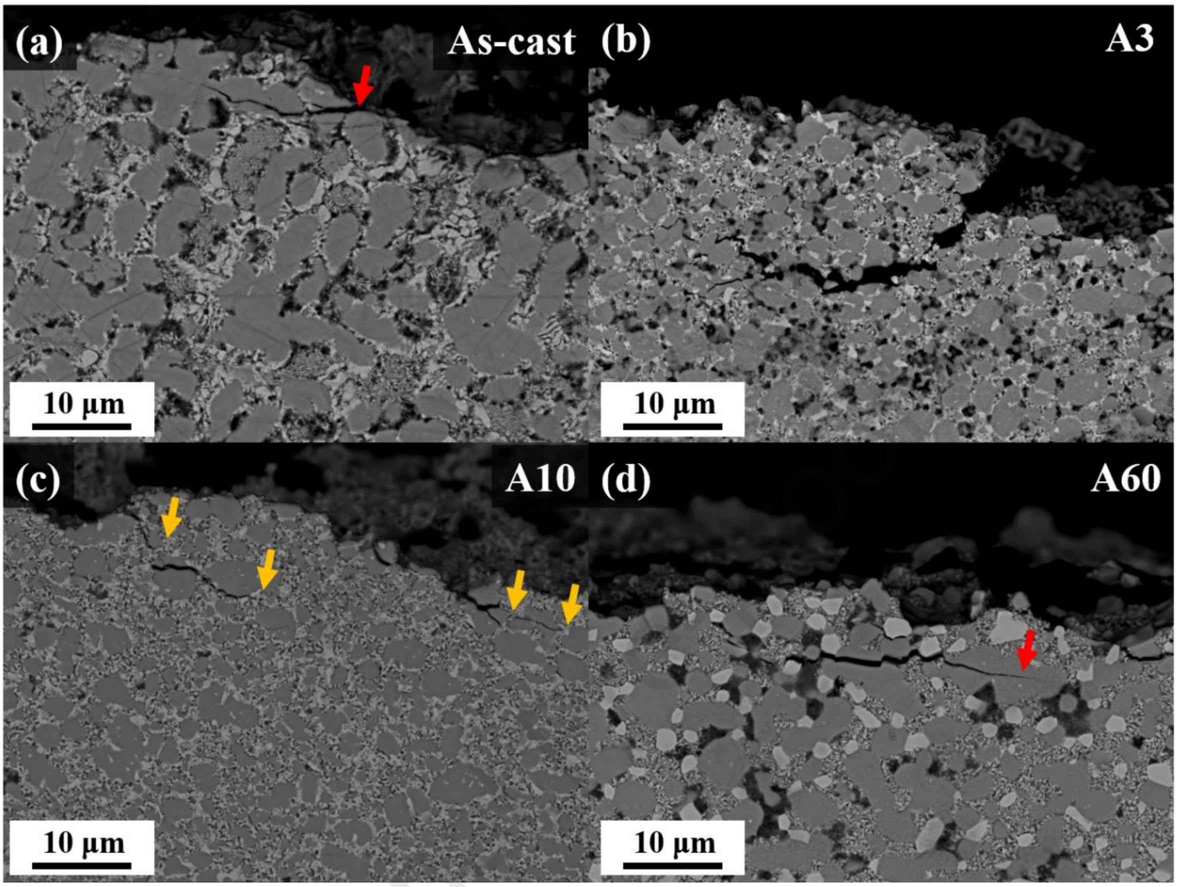

Figure 9. Longitudinal sections of the fractured AlZnCu MEAs: (a) as-cast, (b) A3, (c) A10, and (d) A60 samples.

The combination of strength and ductility in AlZnCu MEAs is remarkable, Particularly considering that deformable Al-based MEAs under tensile stress have not been reported yet. Although tensile properties were previously obtained from modified 5083 alloys, the configurational entropy calculated from the overall composition of these modified 5083 alloys ranged from 0.47R to 0.48R [11]. Therefore, the tensile properties of AlZnCu MEAs represent a cornerstone in deformable Al-based MEA under tensile testing. To compare the mechanical properties of AlZnCu MEA to the Al-MEAs reported in previous studies [7-10], the compressive mechanical properties of the as-cast sample are investigated. The compressive stress-strain curves are displayed in the supplementary file (Fig. S2), which shows a YS of ~487.9 MPa, compressive strength of ~672.2 MPa, and compressive ductility of 9.7% until fracture. Excluding the strain softening region, the compressive ductility is ~3.5%. Figure 10(a) summarizes the compressive mechanical properties of Al-MEAs. The as-cast AlZnCu MEA surpasses the compressive strength level of Al-MEAs with a reasonable compressive ductility. Furthermore, the tensile properties of AlZnCu MEA are compared to those of Al 2xxx alloy series (Fig. 10(b)) [56-61]. Due to a large amount of intermetallic compounds, the AlZnCu MEA shows a lack of ductility compared to the Al 2xxx alloy series. However, the UTS achieved in the present study is comparable with the conventional Al alloys.

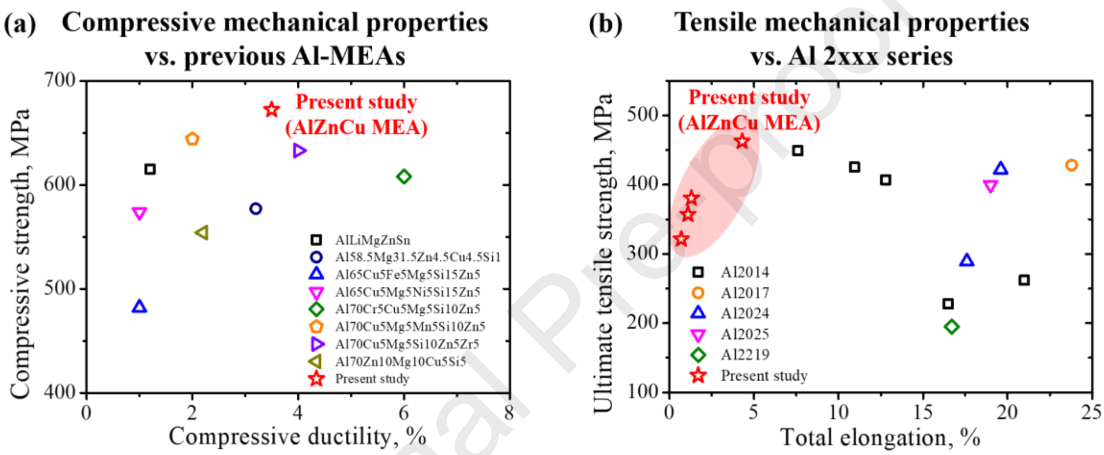

Figure 10. Comparison of (a) compressive mechanical properties versus the other Al-MEAs reported in the previous studies [7-10] and (b) tensile mechanical properties versus the Al-Cu 2xxx alloy series [56-61].

Conclusions

In this work, a new AlZnCu MEA was designed, and tensile mechanical properties were obtained by tailoring thermomechanical processes. The key findings and conclusions are summarized as follows:

1. The new $Al_{40}Zn_{40}Cu_{20}$ MEA was designed based on thermodynamic calculations to possess the multi-phase structure, comprising Al-rich FCC and Zn-rich HCP lamellar structures, with AlCu intermetallic compounds serving as reinforcement materials.

2. The as-cast AlZnCu MEA exhibits brittle fracture, primarily due to coarse AlCu dendrites. However, the HPT process mechanically redistributes the constituent phases on a nanoscale, and subsequent annealing recovers the microstructures. The annealed sample shows ductility of ~4.3% and strength of ~462.5 MPa under tensile stress, achieved by refining the AlCu phases and recovering the deformed microstructure.

The findings of this study on AlZnCu MEA and its thermomechanical processing represent a significant advancement in the field, offering new possibilities for deformable Al-based MEAs. This work may serve as a pivotal milestone in the development of future Al-based MEAs with enhanced tensile properties and opens up new avenues for exploration in this area.

Acknowledgment

This research was supported by the Nano & Material Technology Development Program through the National Research Foundation of Korea (NRF) funded by the Ministry of Science and ICT (RS-2023-00281246).

Competing interests

The authors declare that they have no competing interests.

Data and materials availability

The data that support the findings of this study are available from the corresponding author upon reasonable request.

References

[1] M. Asadikiya, S. Yang, Y. Zhang, C. Lemay, D. Apelian, Y. Zhong, A review of the design of high-entropy aluminum alloys: a pathway for novel Al alloys, J. Mater. Sci. 56 (2021) 12093-12110.

[2] B. Cantor, I.T.H. Chang, P. Knight, A.J.B. Vincent. Microstructural development in equiatomic multicomponent alloys, Mater Sci Eng, A 375e377 (2004) 213e8.

[3] H. Kwon, P. Sathiyamoorthi, G.M. Karthik, A. Zargaran, J. Wang, Y.-U. Heo, S. Harjo, W. Gong, B.-J. Lee, H.S. Kim, High-density nanoprecipitates and phase reversion via maraging enable ultrastrong yet strain-hardenable medium-entropy alloy, Acta Mater. 248 (2023)118810.

[4] B.B. Straumal, A. Korneva, A. Kuzmin, G.A. Lopez, E. Rabkin, A.B. Straumal, G. Gerstein, A.S. Gornakova, The grain boundary wetting phenomena in the Ti-containing high-entropy alloys: A review, Metals 11(11) (2021) 1881.

[5] S. Son, D. Lee, H. Kwon, J. Moon, K.B. Park, A. Kim, J. Choi, J.-H. Jeong, S. Cho, H.S. Kim, Microstructure and mechanical properties of equiatomic Ti-containing medium-entropy alloys, J. Alloy Compd. 935(1) (2023) 168089.

[6] H. Park, J. Lee, R.E. Kim, S. Son, S.Y. Ahn, H.S. Kim, Effect of warm rolling on the structure and tensile properties of a metastable Fe-based medium entropy alloy, Met. Mater. Int. 30 (2024) 585-592.

[7] X. Yang, S.Y. Chen, J.D. Cotton, Y. Zhang, Phase stability of low-density, multi-principal component alloys containing aluminum, magnesium, and lithium, JOM 66 (2014) 2009-2020.

[8] L. Shao, T. Zhang, L. Li, Y. Zhao, J. Huang, P.K. Liaw, Y. Zhang, A low-cost lightweight entropic alloy with high strength, J. Mater. Eng. Perform. 27 (2018) 6648-6656.

[9] J.M. Sanchez, I. Vicario, J. Albizuri, T. Guraya, E.M. Acuna, Design, microstructure and mechanical properties of cast medium entropy aluminium alloys, Sci. Rep. 9 (2019) 6792.

[10] Y. Huang, J. Wen, Y. Liu, Y. Zhao, Effects of electromagnetic frequency on the microstructure and mechanical properties of $Al_{70}Zn_{10}Mg_{10}Cu_5Si_5$ medium entropy alloy, J. Mater. Res. Technol. 17 (2022) 3105-3117.

[11] B. Zhang, P.K. Liaw, J. Brechtl, J. Ren, X. Guo, Y. Zhang, Effects of Cu and Zn on microstructures and mechanical behavior of the medium-entropy aluminum alloy, J. Alloy Compd. 820 (2020) 153092.

[12] S. Son, P. Asghari-Rad, J. Choi, A. Kim, J.-H. Jeong, S. Cho, H.S. Kim, Design and mechanical properties of body-centered cubic AlVCr medium-entropy aluminum alloys, J. Mater. Res. Technol. 24 (2023) 7302-7312.

[13] W.B. Zhou, G.B. Teng, C.Y. Liu, H.Q. Qi, H.F. Huang, Y. Chen, H.J. Jiang, Microstructures and mechanical properties of binary Al-Zn alloys fabricated by casting and heat treatment, J. Mater. Eng. Perform. 26 (2017) 3977-3982.

[14] U. Bansal, M.P. Singh, S.K. Sinha, D.K. Sahu, S. Mondol, S.K. Makineni, A. Paul, K. Chattopadhyay, Strength and stability through variable micro segregation behaviour of Ta and Zr solutes at intermetallic interfaces in Al-Cu alloys, Acta Mater. 259 (2023) 119254.

[15] T.K. Akopyan, P.K. Shurkin, N.V. Letyagin, F.O. Milovich, A.S. Fortuna, A.N. Koshmin, Structure and precipitation hardening response in a cast and wrought Al-Cu-Sn alloy, Mater. Lett. 300 (2021) 130090.

[16] G. Wang, B. Lin, D.-D. Lu, S.-X. Deng, G.-J. Zeng, X.-F. Cai, J.-F. Li, D.-Y. Liu, Effect of aging precipitate on ductility anisotropy and low cycle fatigue behavior of AA2195 Al-Li alloy, Met. Mater. Int. 29 (2023) 2166-2181.

[17] Y. Huang, P. Bazarnik, D. Wan, D. Luo, P.H.R. Pereira, M. Lewandowska, J. Yao, B.E. Hayden, T.G. Langdon, The fabrication of graphene-reinforced Al-based nanocomposites using high-pressure torsion, Acta Mater. 164 (2019) 499-511.

[18] Z. Li, G. Wu, Y. Liu, J. Yu, Grain refinement and second phases evolution of Mg-13Gd-4Y-2Zn-0.4Zr sheet during processing by rotary forward extrusion, Met. Mater. Int. 29 (2023) 3249-3272.

[19] R.L. Fleischer, Substitutional solution hardening, Acta Metall. 11(3) (1963) 203-209.

[20] V.A. Lubarda. On the effective lattice parameter of binary alloys, Mech. Mater. 35 (2003) 53-68.

[21] S.Z. Hang, E.-A. Choi, H.W. Park, S.H. Lim, J. Lee, J.H. Ahn, N.-M. Hwang, K. Kim,

Simultaneous increase in strength and ductility by decreasing interface energy between Zn and Al phases in cast Al-Zn-Cu alloy, Sci. Rep. 7 (2017) 12195

[22] B. Zhang, P.K. Liaw, J. Brechtl, J. Ren, X. Guo, Y. Zhang, Effects of Cu and Zn on microstructures and mechanical behavior of the medium-entropy aluminum alloy, J. Alloy Compd. 820 (2020) 153092.

[23] Q. Meng, G.S. Frankel, Effect of Cu Content on Corrosion Behavior of 7xxx Series Aluminum Alloys, J. Electrochem. Soc. 151 (2004) B271.

[24] I. Toda-Caraballo, P.E.J. Rivera-Diaz-del-Castillo. Modelling solid solution hardening in high entropy alloys, Acta Mater. 85 (2015) 14-23.

[25] J. Moon, J.M. Park, J.W. Bae, H.-S. Do, B.-J. Lee, H.S. Kim, A new strategy for designing immiscible medium-entropy alloys with excellent tensile properties, Acta Mater. 193 (2020) 71-82.

[26] S. Son, J. Moon, H. Kwon, P. Asghari-Rad, H. Kato, H.S. Kim, Novel Co-Cu-based immiscible medium-entropy alloys with promising mechanical properties, Metals 11 (2021) 238.

[27] A. Takeuchi, A. Inoue. Calculations of mixing enthalpy and mismatch entropy for ternary amorphous alloys, Mater. Trans. JIM 40(11) (2000) 1372-1378.

[28] B. Legendre, Y. Feutelais, J.M. San Juan, I. Hurtado, Enthalpy of formation of the ternary τ′ phase in the Al–Cu–Zn system. J. Alloy Compd. 308(1-2) (2000) 216-220.

[29] S. Son, J. Lee, P. Asghari-Rad, R.E. Kim, H. Park, J.-I. Jang, W. Chen, Y.-U. Heo, H.S. Kim, Hierarchically heterogeneous microstructure and mechanical behavior of the multi-materials prepared by powder severe plastic deformation, Mater. Res. Lett. 11(11) (2023) 915-924.

[30] Y. Ivanisenko, W. Lojkowski, R.Z. Valiev, H.J. Fecht, The mechanism of formation of nanostructure and dissolution of cementite in a pearlitic steel during high pressure torsion. Acta Mater. 51(18) (2003) 5555–5570.

[31] S. Son, P. Asghari-Rad, A. Zargaran, W. Chen, H.S. Kim, Superlative room temperature and cryogenic tensile properties of nanostructured CoCrFeNi medium-entropy alloy fabricated

by powder high-pressure torsion, Scr. Mater. 213 (2022) 114631.

[32] J. Oh, S. Son, H.S. Kim, J.B. Seol, H. Sung, J.G. Kim, Mechanical properties and microstructural evolutions of high-pressure torsion-processed Al7068 alloy, Korean J. Met. Mater. 61(1) (2022) 1-8.

[33] S.A.H. Kahnooj, M. Vaseghi, M. Sameezadeh, Softening and microstructure evolution of pure copper disks processed by high pressure torsion, Met. Mater. Int. 28 (2022) 2646-2651.

[34] X. Gao, Y. Lu, B. Zhang, N. Liang, G. Wu, G. Sha, J. Liu, Y. Zhao, Microstructural origins of high strength and high ductility in an $AlCoCrFeNi_{2.1}$ eutectic high-entropy alloy, Acta Mater. 141 (2017) 59-66.

[35] A.L. Ortiz, L. Shaw, X-ray diffraction analysis of a severely plastically deformed aluminum alloy, Acta Mater. 52(8) (2004) 2185-2197.

[36] S.-M. Liang, H.-M. Hsiao, R. Schmid-Fetzer, Thermodynamic assessment of the Al–Cu–Zn system, part I: Cu–Zn binary system, Calphad 51 (2015) 224-232.

[37] Y. Wang, J. Gao, Y. Ren, V.D. Andrade, A.J. Shahani, Formation of a three-phase spiral structure due to competitive growth of a peritectic phase with a metastable eutectic, JOM 72 (2020) 2965-2973.

[38] S. Maity, D. Kr. Chanda, R. Ramasamy, B.K. Show, J. Eckert, S. Bera, Evolution of bimodal microstructure and high-temperature wear resistance of Al-Cu-Ni alloy, Metall. Mater. Trans. A 51 (2020) 109-115. https://doi.org/10.1007/s11661-019-05518-0.

[39] S. Xi, G. Ma, L. Li, Y. Zhang, X. Yu, Y. Li, R. Zhou, Microstructures and mechanical properties of 4 wt% TiB_2/Al-Si-Cu-Zn (T6) composite thin-walled shell housing fabricated by high pressure die casting, Mater. Res. Express 8 (2021) 036514. DOI 10.1088/2053-1591/abecae.

[40] D. Nguyen-Manh, D.G. Pettifor, Electronic structure, phase stability and elastic moduli of AB transition metal aluminides, Intermetallic 7(10) (1999) 1095-1106. https://doi.org/10.1016/S0966-9795(99)00040-0.

[41] F. Sun, G. Zhang, H. Liu, H. Xu, Y. Fu, D. Li, Effect of transition-elements substitution on mechanical properties and electronic structures of B2-AlCu compounds, Results Phys. 21

(2021) 103765. https://doi.org/10.1016/j.rinp.2020.103765.

[42] E.V. Shalaeva, N.I. Medvedeva, I.R. Shein, Ab Initio calculations of the stability and structural defects of the B2 $Cu_xFe_{1-x}Al$ phases, Phys. Solid State 49 (2007) 1253-1258. https://doi.org/10.1134/S1063783407070098.

[43] F. Lanzini, P.H. Gargano, P.R. Alonso, G.H. Rubiolo, First-principles study of atomic ordering in bcc Cu–Al, Model. Simul. Mater. Sci. Eng. 19 (2011) 015008. DOI 10.1088/0965-0393/19/1/015008.

[44] X. Zhou, R.D. Kamachali, B.L. Boyce, B.G. Clark, D. Raabe, G.B. Thompson, Spinodal decomposition in nanocrystalline alloys, Acta Mater. 215 (2015) 117054. https://doi.org/10.1016/j.actamat.2021.117054.

[45] S. Venkatesan, M.A. Xavior. Analysis of mechanical properties of aluminum alloy metal matrix composite by squeeze casting – A review, Mater. Today Proc. 5 (2018) 11175-11184.

[46] K. Luo, S. Liu, H. Xiong, Y. Zhang, C. Kong, H. Yu, Mechanical properties and strengthening mechanism of aluminum matrix composites reinforced by high-entropy alloy particles, Met. Mater. 28 (2022) 2811-2821.

[47] R. Tao, Y. Zhao, G. Chen, X. Kai, Effects of ZrB_2 Nanoparticles on the microstructures and tensile properties of a hot extruded In-situ AA6111 composite, Met. Mater. Int. 28 (2022) 3145-3159.

[48] Z. Mao, J. Xie, A. Wang, W. Wang, D. Ma, Interfacial Characterization and Bonding Properties of Copper/Aluminum Clad Sheets Processed by Horizontal Twin-Roll Casting, Multi-Pass Rolling, and Annealing, Metals 8(8) (2018) 645.

[49] Y. Xiao, H. Besharatloo, B. Gan, X. Maeder, R. Spolenak, J.M. Wheeler, Combinatorial investigation of Al–Cu intermetallics using small-scale mechanical testing, J. Alloy Compd. 822 (2020) 153536.

[50] L. Chen, X. Ma, Z. Ma, D. Lu, B. Hou, Study on microstructure and corrosion resistance of high-hardness Zn-1.0Cu-1.0Ti alloy, Mater. Charact. 178 (2021) 111283.

[51] F. Wang, D. Eskin, J. Mi, C. Wang, B. Koe, A. King, C. Reinhard, T. Connolley, A synchrotron X-radiography study of the fragmentation and refinement of primary intermetallic

particles in an Al-35 Cu alloy induced by ultrasonic melt processing, Acta Mater. 141 (2017) 142-153.

[52] J.L. Qi, Z.Y. Wang, J.H. Lin, T.Q. Zhang, A.T. Zhang, J. Cao, L.X. Zhang, J.C. Feng, Graphene-enhanced Cu composite interlayer for contact reaction brazing aluminum alloy 6061, Vacuum 136 (2017) 142-145.

[53] A. Needleman, V. Tvergaard, An analysis of ductile rupture modes at a crack tip, J. Mech. Phys. Solids 35(2) (1987) 151-183.

[54] A Neogi, R. Janisch, Twin-boundary assisted crack tip plasticity and toughening in lamellar γ-TiAl, Acta Mater. 213 (2021) 116924.

[55] G. Niu, H.S. Zurob, R.D.K. Misra, Q. Tang, Z. Zhang, M.-T. Nguyen, L. Wang, H. Wu, Y. Zou, Superior fracture toughness in a high-strength austenitic steel with heterogeneous lamellar microstructure, Acta Mater. 226 (2022) 117642.

[56] MK. Pathak, A. Joshi, K.K.S. Mer, Evaluating tensile properties and fracture toughness of Al 2014 alloy processed by different rolling methods, Mater. Res. Exp. 6 (2019) 105012.

[57] M.R. Roshan, M. Mirzaei, S.A.J. Jahromi, Microstructural characteristics and tensile properties of nano-composite Al 2014/4 wt.% Al2O3 produced from machining chips, J. Alloy Compd. 569 (2013) 111-117.

[58] H.J. Liu, H. Fujii, M. Maeda, K. Nogi, Tensile properties and fracture locations of friction-stir-welded joints of 2017-T351 aluminum alloy, J. Mater. Proc. Technol. 142(3) (2003) 692-696.

[59] H. Aydin, A. Bayram, A. Uguz, K.S. Akay, Tensile properties of friction stir welded joints of 2024 aluminum alloys in different heat-treated-state, Mater. Des. 30(6) (2009) 2211-2221.

[60] V. Ramana G, B. Yelamasetti, V. Vardhan T, Study on weldability and effect of post heat treatment on mechanical and metallurgical properties of dissimilar AA 2025, AA 5083 and AA7075 GTAW weld joints, Mater. Today Proc. 46(1) (2021) 878-882.

[61] G. Chu, L. Sun, Y. Lin, Effect of local post weld heat treatment on tensile properties in friction stir welded 2219-O Al alloy, J. Mater. Eng. Perform. 26 (2017) 5425-5431.

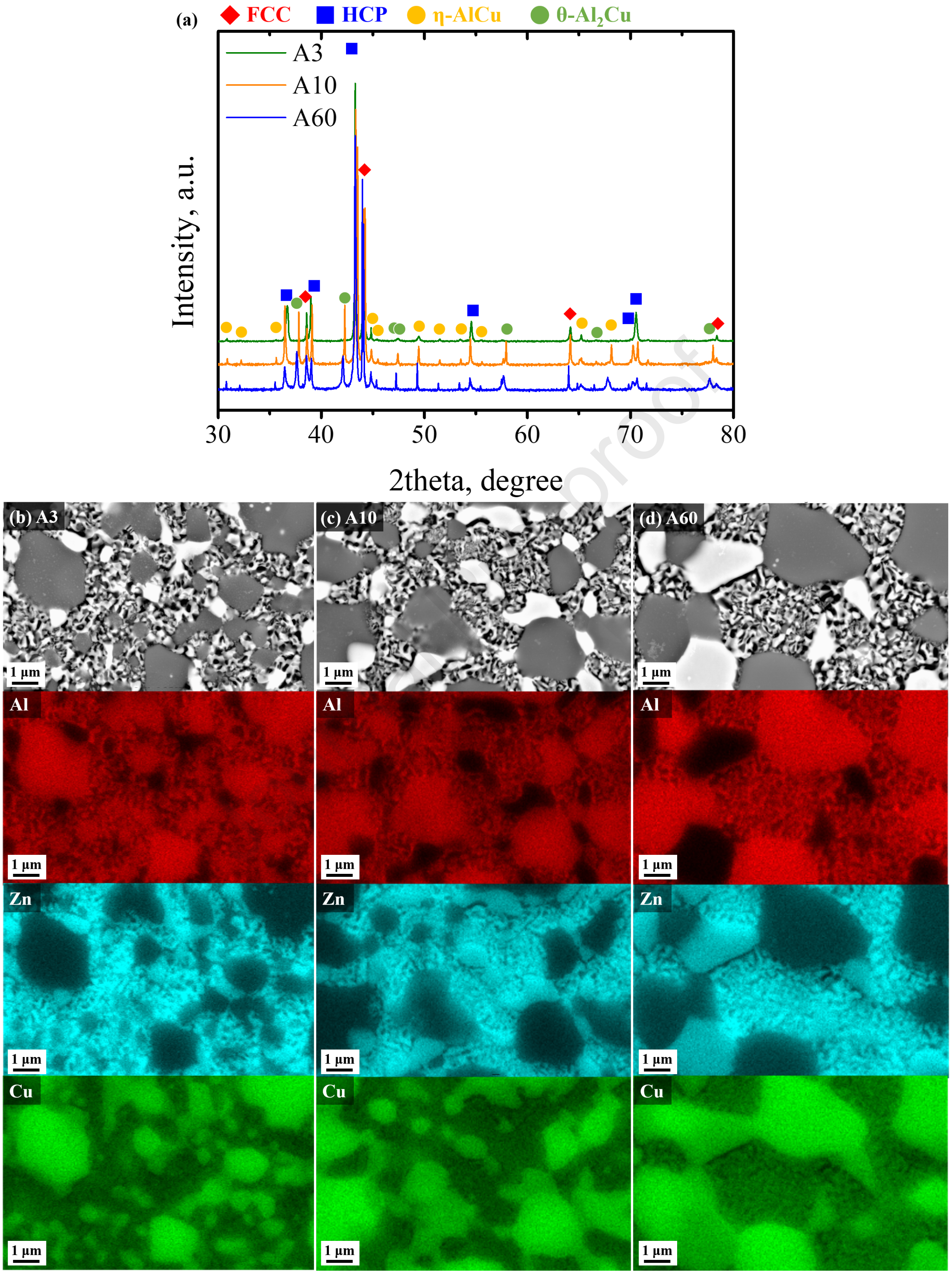

(a)
FCC
HCP
η-AlCu
θ-Al2Cu
A3
A10
A60
Intensity, a.u.
30
40
50
60
70
80
2theta, degree
(b) A3
(c) A10
(d) A60
Al
Zn
Cu
1 μm

Declaration of interests

☒ The authors declare that they have no known competing financial interests or personal relationships that could have appeared to influence the work reported in this paper.

☐ The authors declare the following financial interests/personal relationships which may be considered as potential competing interests: